



SEISMIC-ENVIRONMENT-BASED SIMULATION OF NEAR-FAULT GROUND MOTIONS

Qiang FU¹ and Charles MENUN²

SUMMARY

The critical structural response caused by near-fault ground motions is often influenced by the presence of a velocity pulse in the fault-normal component. This paper describes a procedure for simulating fault-normal near-fault ground motions for a specified seismic environment (i.e., the magnitude, distance and faulting mechanism of an earthquake and the soil conditions at the site). The proposed ground motion velocity model is defined by a number of parameters that, for a specified near-fault record, are determined by a nonlinear regression. This paper derives predictive relationships for these parameters based on the seismic environment of a site using results obtained from a series of regression analyses performed on an ensemble of recorded fault-normal near-fault ground motions. The ability and limitations of the proposed simulation procedure for structural analysis and design are evaluated by comparing the displacement demands in linear and nonlinear single-degree-of-freedom systems caused by the ensemble of recorded ground motions and their simulations. The results of these analyses indicate that, on average, the simulated and recorded responses agree at periods greater than 1.5s; however, at shorter periods, discrepancies as large as 20% are observed.

INTRODUCTION

For structures located within 15 km of a rupturing fault, damage is often incurred during one or two cycles of severe inelastic deformations that coincide with a large amplitude velocity pulse in the fault-normal component of the ground motion. Because such ground motions impose severe demands on structures, there is an increasing demand from the professional practice for accelerograms that can be used as input to nonlinear time-history analyses of structures located in near-fault environments. Unfortunately, only a small number of ground motions have been recorded in such environments, so there is a need for procedures that can be used to generate simulated near-fault ground motions to augment the historical database.

In this paper, we describe an analytical model for the fault-normal velocity pulse that is similar to models previously proposed by Menun [1] and Mavroeidis [2]. While it has been demonstrated that such models can accurately predict the response of structures whose fundamental period of vibration is greater than or

¹ Doctoral candidate, Stanford University. Email: qfu@stanford.edu

² Assistant Professor, Stanford University. Email: menun@stanford.edu

equal to the period of the velocity pulse, for structures that have shorter natural periods, these models tend to underestimate the displacement demands due to their inability to reproduce the high frequency content of the recorded ground motions. To address this problem, the ground motion model proposed in this paper includes a stochastic component to represent the high frequency content.

The proposed simulation procedure utilizes several parameters to control the temporal and frequency domain characteristics of the resulting ground motion. Empirical relationships that can be used to predict appropriate values for these model parameters for a given seismic environment (the magnitude, distance and faulting mechanism of the earthquake and the site soil conditions) are derived from regression analyses performed on an ensemble of recorded fault-normal near-fault ground motions. To specify the high frequency content of the simulated records, readily available attenuation relationships for response spectrum ordinates and Arias duration are used to calibrate the parameters of the stochastic component of the model.

To assess the suitability of the proposed simulation procedure, a series of nonlinear time-history analyses are performed on linear and nonlinear single-degree-of-freedom systems using the ensemble of recorded ground motions and an ensemble of simulated ground motions. In general, it is found that the ensemble means of the simulated and recorded responses agree at periods $T > 1.5$ s; however, discrepancies as large as 20% are observed for $T < 1.5$ s.

GROUND MOTION MODEL AND SIMULATION PROCEDURE

Velocity pulse model

A distinct large-amplitude velocity pulse is often seen in the fault-normal component of the ground motion recorded near a rupturing fault. Seismologists have determined that this phenomenon is caused by the superposition of seismic shear waves in the direction of the rupture propagation when the rupture velocity is approximately the same as the shear wave velocity (e.g., Somerville [3]). Plotted in Figure 1 are synthetic ground motions generated by the Haskell source model [4] assuming forward directivity site conditions. The velocity pulses that are apparent in these synthetic ground motions are idealized in this paper as

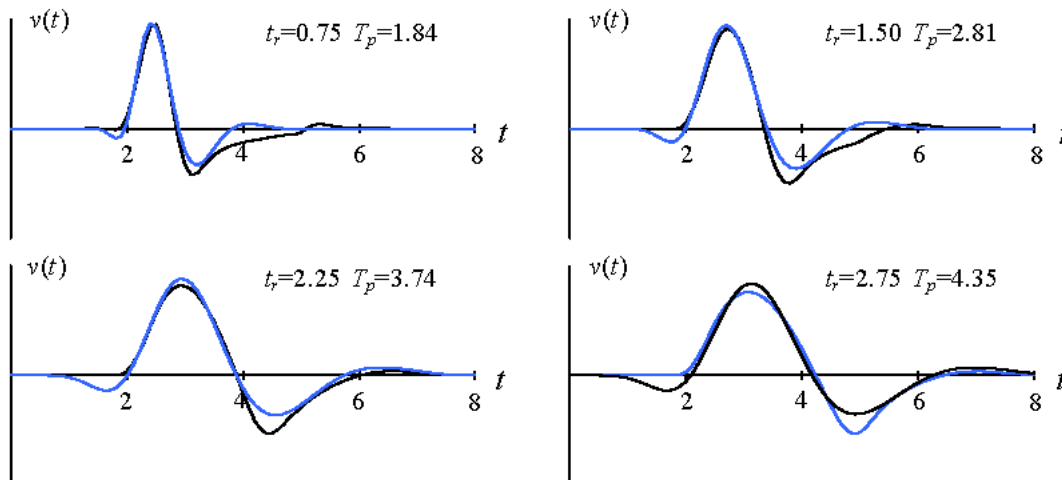


Figure 1. Ground velocity obtained from the Haskell model (black lines) and proposed velocity model (blue lines).

$$v_p(t) = \begin{cases} V_p \exp\{1 - \alpha(t - t_p) - \exp[-\alpha(t - t_p)]\} \sin[2\pi(t - t_0)/T_p] & t_0 \leq t \leq t_0 + 2T_p \\ = 0 & \text{otherwise,} \end{cases} \quad (1)$$

where V_p and T_p characterize the amplitude and period of the velocity pulse, respectively, t_0 specifies the time at which the pulse starts, α is shape parameter that defines the growth and decay of the velocity pulse and $t_p = t_0 + 0.75T_p$ is the time at which the peak velocity occurs. Using the iterative procedure described by Menun [1], the parameters of the ground velocity model defined by (1) are calibrated to fit the synthetic ground motions plotted in Figure 1. By superimposing the resulting velocity traces obtained from (1) over their Haskell counterparts in Figure 1, we can see that the proposed ground velocity model can capture the salient features of the seismological source model.

Table 1a. Recorded ground motions on rock and fitted ground motion model parameters.

| Earthquake | M_w | Station | R (km) | PGV (cm/s) | V_p (cm/s) | T_p (s) | α |
|--------------------|-------|---------------------------|-------------|---------------|-----------------|--------------|----------|
| N. Palm Springs | 6.0 | North Palm Springs | 8.2 | 73.5 | 58.9 | 1.26 | -2.28 |
| N. Palm Springs | 6.0 | Desert Hot Springs | 8.0 | 26.9 | -22.0 | 1.38 | 2.05 |
| N. Palm Springs | 6.0 | Whitewater Trout Farm | 7.3 | 35.8 | -27.3 | 0.63 | 0.63 |
| Parkfield | 6.1 | Temblor pre - 1969 | 9.9 | 22.4 | -12.9 | 0.39 | 0.00 |
| Morgan Hill | 6.2 | Anderson Dam | 2.6 | 27.3 | -27.3 | 0.49 | -5.96 |
| Morgan Hill | 6.2 | Gilroy Array # 6 | 11.8 | 36.5 | -32.0 | 1.04 | 1.70 |
| Morgan Hill | 6.2 | Coyote Lake Dam | 0.1 | 67.1 | -46.8 | 0.76 | -0.93 |
| San Fernando | 6.6 | Pacoima dam | 2.8 | 114.3 | -103.2 | 1.38 | 1.95 |
| Superstition Hills | 6.7 | Parachute Test site | 0.7 | 106.8 | 105.9 | 2.12 | 1.29 |
| Northridge | 6.7 | Rinaldi Receiving | 7.1 | 173.1 | 165.0 | 1.16 | 3.13 |
| Northridge | 6.7 | Newhall-W.Pico Canyon Rd. | 7.1 | 87.7 | 101.5 | 2.18 | -1.48 |
| Northridge | 6.7 | Pacoima Dam Downstream | 8.0 | 49.6 | -46.1 | 0.48 | 6.58 |
| Northridge | 6.7 | Pacoima Kagel Canyon | 8.2 | 56.2 | -50.1 | 0.72 | 3.09 |
| Northridge | 6.7 | LA Dam | 2.6 | 75.1 | 76.3 | 1.42 | 3.16 |
| Nahanni, Canada | 6.8 | Site 1 | 6.0 | 45.8 | 17.4 | 3.25 | 0.78 |
| Nahanni, Canada | 6.8 | Site 2 | 8.0 | 23.9 | 21.4 | 1.20 | -8.75 |
| Loma Prieta | 6.9 | Gilroy Array #1 | 11.2 | 38.5 | -36.9 | 4.24 | -11.0 |
| Loma Prieta | 6.9 | Gilroy-Gavilan Coll. | 11.6 | 30.8 | 20.6 | 1.77 | -2.56 |
| Loma Prieta | 6.9 | Saratoga-Aloha Ave. | 13.0 | 55.6 | -50.6 | 2.25 | -1.77 |
| Loma Prieta | 6.9 | Saratoga-W Valley Coll. | 13.7 | 71.3 | -70.7 | 2.16 | -4.19 |
| Loma Prieta | 6.9 | Los Gatos | 3.5 | 173.0 | 109.2 | 3.21 | 0.50 |
| Loma Prieta | 6.9 | Lexington Dam | 6.3 | 178.8 | 156.2 | 1.81 | -1.93 |
| Kobe, Japan | 6.9 | KJMA | 0.6 | 95.7 | -78.3 | 0.86 | 0.00 |
| Kobe, Japan | 6.9 | Kobe Station | 3.4 | 160.3 | -118.1 | 0.90 | 0.00 |
| Landers | 7.3 | Lucerne Valley | 1.1 | 136.0 | -68.2 | 5.54 | -0.14 |
| Kocaeli, Turkey | 7.4 | Gebze | 17.0 | 50.3 | -41.6 | 6.47 | 0.53 |

The corresponding idealized ground acceleration, which is found by differentiating (1), can be written as

$$a_p(t) = \begin{cases} V_p A_p(t) \cos[2\pi(t-t_0)/T_p - \varphi] & t_0 \leq t \leq t_0 + 2T_p \\ = 0 & \text{otherwise} \end{cases} \quad (2)$$

where

$$A_p(t) = \exp\{1 - \alpha(t-t_p) - \exp[-\alpha(t-t_p)]\} \sqrt{\{-\alpha + \alpha \exp[-\alpha(t-t_p)]\}^2 + (2\pi/T_p)^2} \quad (3)$$

is the modulating function for acceleration, and

$$\varphi = \arctan \frac{-\alpha + \alpha \exp[-\alpha(t-t_p)]}{2\pi/T_p}. \quad (4)$$

We remark that the phase angle φ has a very subtle effect on the time, $t_p^{(a)}$, at which the peak acceleration occurs; thus, $t_p^{(a)}$ is not the same as t_p but it is very close to t_p .

Table 1b. Recorded ground motions on soil and fitted ground motion model parameters.

| Earthquake | M_w | Station | R (km) | PGV (cm/s) | V_p (cm/s) | T_p (s) | α |
|--------------------|-------|-----------------------------|-------------|---------------|-----------------|--------------|----------|
| Whittier Narrows | 6.0 | Bell Gardens – Jaboneria | 9.8 | 19.1 | -20.5 | 0.71 | 0.71 |
| Whittier Narrows | 6.0 | Santa Fe Springs – E Joslin | 10.8 | 23.7 | 15.5 | 0.70 | -2.71 |
| Parkfield | 6.1 | Station 2 (Cholame #2) | 0.1 | 75.0 | -57.0 | 1.88 | -1.68 |
| Coalinga | 6.4 | Pleasant Valley P.P.-Bldg | 8.5 | 57.9 | -54.3 | 0.70 | -3.04 |
| Superstition Hills | 6.7 | El Centro Imp. Co. Cent | 13.9 | 51.9 | 43.2 | 2.41 | 1.25 |
| Northridge | 6.7 | Canoga Park -Topanga Can | 15.8 | 53.5 | -40.3 | 2.02 | -1.12 |
| Northridge | 6.7 | Canyon Cty-W Lost Cany | 13.0 | 53.5 | 27.2 | 1.89 | 0.89 |
| Northridge | 6.7 | Jensen Filter Plant | 6.2 | 104.5 | 69.8 | 2.83 | -0.40 |
| Northridge | 6.7 | Newhall – Fire Station | 7.1 | 120.9 | -106.8 | 0.93 | 3.54 |
| Northridge | 6.7 | Sepulveda VA | 8.9 | 65.5 | 19.1 | 2.99 | 0.00 |
| Northridge | 6.7 | Sylmar Converter Station | 6.2 | 130.3 | -74.6 | 2.88 | 0.52 |
| Northridge | 6.7 | Sylmar Converter East | 6.1 | 116.5 | -60.6 | 3.05 | 0.67 |
| Northridge | 6.7 | Sylmar Olive View Med FF | 6.4 | 123.1 | 58.5 | 2.53 | -0.32 |
| Loma Prieta | 6.9 | Gilroy-Historic Bldg. | 12.7 | 31.9 | -21.0 | 1.54 | -0.78 |
| Loma Prieta | 6.9 | Gilroy Array #2 | 12.7 | 45.7 | -31.7 | 1.43 | 0.47 |
| Loma Prieta | 6.9 | Gilroy Array #3 | 14.4 | 49.3 | 34.8 | 1.79 | 2.20 |
| Loma Prieta | 6.9 | Gilroy Array #4 | 16.1 | 35.7 | 20.9 | 1.37 | 0.00 |
| Erizincan | 6.9 | Erizincan | 2.0 | 120.2 | 92.6 | 2.31 | 1.32 |
| Kobe, Japan | 6.9 | Port Island | 6.6 | 100.3 | -97.8 | 2.34 | -1.27 |
| Kobe, Japan | 6.9 | Takatori Station | 4.3 | 173.8 | 144.5 | 2.11 | 1.02 |
| Kocaeli, Turkey | 7.4 | Duzce | 12.7 | 58.8 | -56.2 | 4.59 | 0.70 |
| Kocaeli, Turkey | 7.4 | Yarimca | 2.6 | 69.5 | 76.9 | 4.27 | 0.57 |
| Chi-Chi, Taiwan | 7.6 | TCU075 | 1.5 | 88.3 | 88.8 | 5.01 | -0.63 |
| Chi-Chi, Taiwan | 7.6 | TCU129 | 1.2 | 60.0 | 40.2 | 7.41 | -0.44 |
| Chi-Chi, Taiwan | 7.6 | TCU065 | 1.0 | 92.6 | 96.9 | 4.73 | 0.35 |
| Chi-Chi, Taiwan | 7.6 | TCU076 | 2.0 | 62.6 | 42.7 | 4.15 | 0.75 |

Using the iterative procedure mentioned above, the ground velocity model defined by (1) is fit to each member of an ensemble of 52 recorded fault-normal near-fault ground velocities listed in Tables 1a and 1b. The fitted model parameters V_p , T_p , and α for each ground motion are summarized in Tables 1a and 1b along with the moment magnitude of the event, M_w , the recorded peak ground velocity, PGV, and the closest distance to the fault rupture, R .

To demonstrate typical fault-normal ground velocities generated by the model, four recorded ground velocities and their fitted pulse models are plotted in Figure 2. Also shown in this figure are the corresponding accelerations obtained by differentiating the velocity records and their pseudo-acceleration response spectra. We remark that the ground motions plotted in Figure 2 are representative of the entire

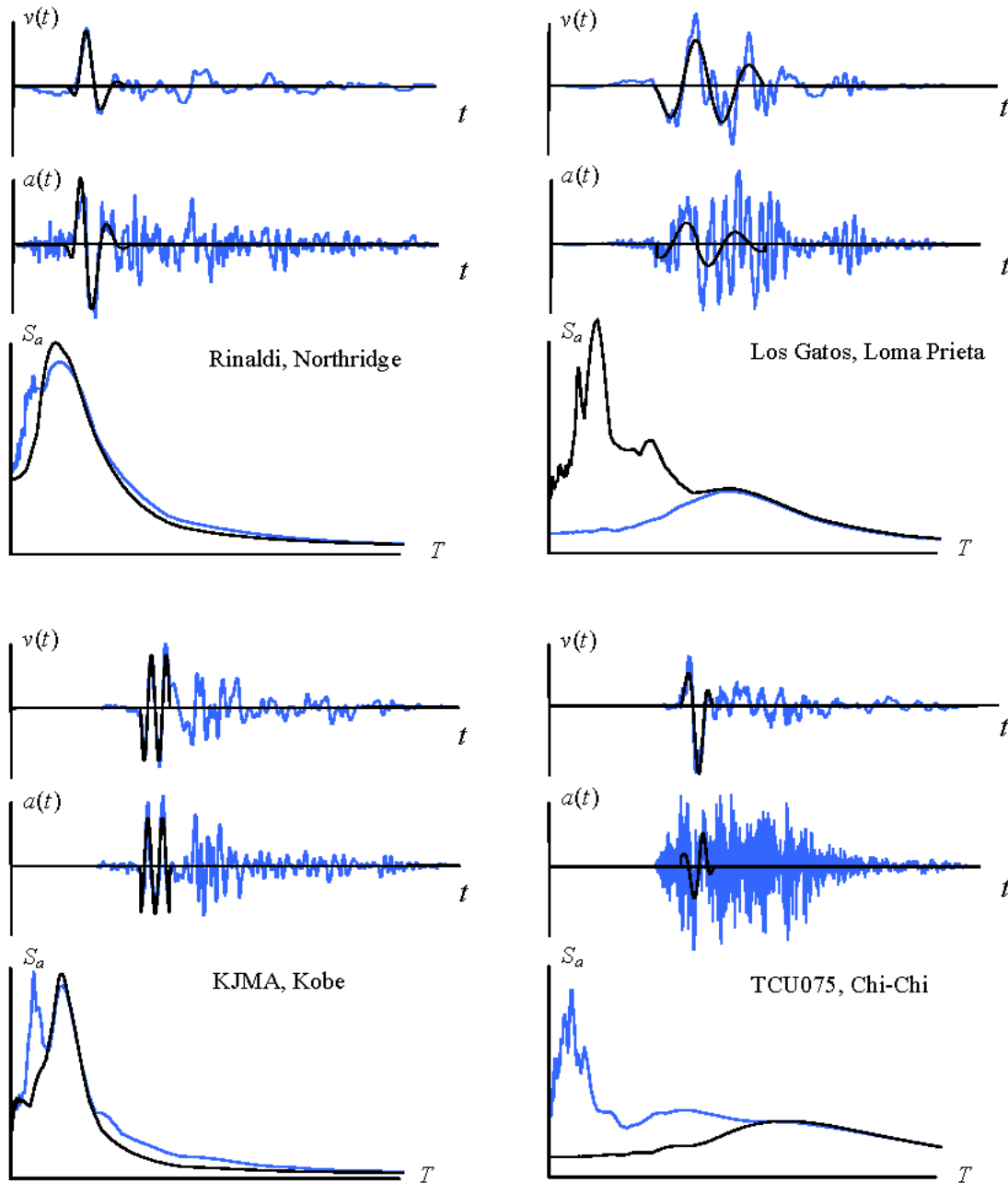


Figure 2. The proposed velocity pulse model (black lines) fitted to the records (blue lines).

High frequency content model

Once the velocity pulse is found for a given near-fault record, the high frequency content can be readily obtained. If we let $a_g(t)$ denote the recorded acceleration, then we can define the acceleration associated with the high frequency content as

$$a_n(t) = a_g(t) - a_p(t), \quad (5)$$

where $a_p(t)$ is defined by (2). As mentioned above, to generate realistic simulations of fault-normal near-fault ground motions we need a model for $a_n(t)$ that can be superimposed on the velocity pulse model. It is known that the high frequency content of an earthquake ground motion is the result of sudden changes in the rupture velocity and slip amplitude. Since these details are unpredictable and stochastic, deterministic methods that convolve the source function with either synthetic or empirical Green's function cannot be used to simulate high frequencies. Thus, we adopt the stochastic model

$$a_n(t) = A_n(t) \sum_{k=1}^{n_\omega} B_k \cos(\omega_k t + \vartheta_k), \quad (6)$$

to simulate the high frequency content, where ω_k , $k = 1, 2, \dots, n_\omega$ is a set of equally spaced frequencies that are included in the sinusoidal superposition, ϑ_k are uniformly distributed random phase angles over $[0, 2\pi)$, B_k are coefficients that define the relative strengths of the different frequencies used in the simulation of $a_n(t)$ and $A_n(t)$ is a modulating function that characterizes the temporal variation in the intensity of the high frequency accelerations.

Based on careful examinations of the 52 near-fault ground motions included in this study, we assume

$$A_n(t) = \exp\{1 - \beta(t - t_n) - \exp[-\beta(t - t_n)]\} \sqrt{\{-\beta + \beta \exp[-\beta(t - t_n)]\}^2 + (2\pi/T_p)^2}, \quad (7)$$

which has a form that is identical to (3). Note that in (7), β and t_n serve the same purposes as α and t_p in (3). In particular, β is a shape factor that defines the growth and decay of the high frequency accelerations and $t_n \approx t_n^{(a)}$, the time at which the peak high frequency accelerations of a realization occur. The data presented in Figure 3a suggests a relatively strong correlation exists between $t_p^{(a)}$ and $t_n^{(a)}$ for the ground motions considered in this study. Recall that $t_p \approx t_p^{(a)}$, as indicated by Figure 3b. Consequently, we assume $t_n = t_p$. Additionally, β is found to be related to the Arias duration, t_d , between the times at which 5% and 95% of the Arias intensity of a recorded accelerogram are realized; namely,

$$\beta \approx \frac{2.5}{t_d}. \quad (8)$$

Using the above relationships for t_n and β , the modulating functions for the high frequency content of four

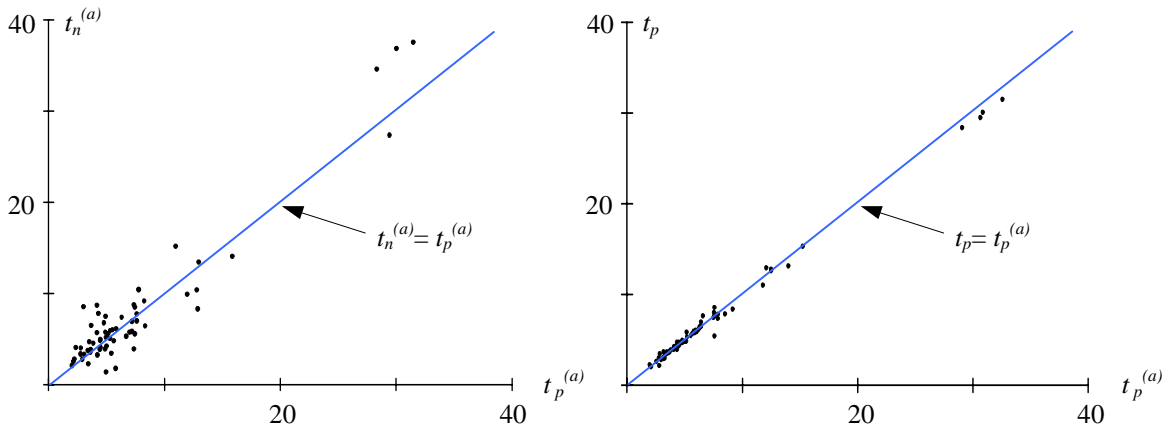


Figure 3a. Correlation between $t_p^{(a)}$ and $t_n^{(a)}$.

Figure 3b. Correlation between t_p and $t_p^{(a)}$.

representative accelerograms from the ensemble of 52 are plotted in Figure 4. It is evident from this figure that the modulating functions match the temporal variation of the high frequency accelerations well. We remark that Figure 4 indicates that $A_n(t)$ does not have a pronounced stationary strong motion phase. This is in contrast to the modulating functions commonly assumed for far-field ground motions that are usually characterized by an initial build up, a relatively long stationary phase, and a gradually decaying tail.

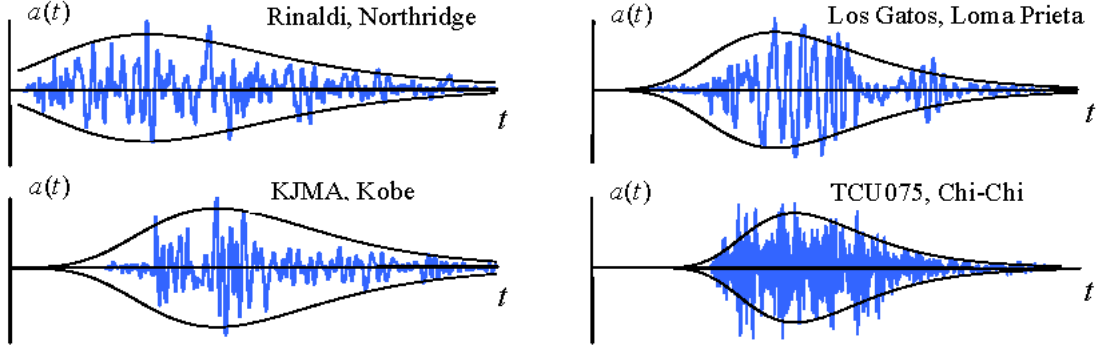


Figure 4. The high frequency accelerations and modulating functions.

Simulation procedure

To generate the ensemble of ground motions for a given near-fault environment, we superimpose the velocity pulse and high frequency content models described in the previous sections to yield

$$\begin{aligned}
 a_s(t) &= a_p(t) + a_n(t) \\
 &= V_p A_p(t) \cos[2\pi(t-t_0)/T_p - \varphi] + A_n(t) \sum_{k=1}^{n_\omega} B_k \cos(\omega_k t + \vartheta_k) \quad t_0 \leq t \leq t_0 + 2T_p \quad (9) \\
 &= A_n(t) \sum_{k=1}^{n_\omega} B_k \cos(\omega_k t + \vartheta_k) \quad \text{otherwise.}
 \end{aligned}$$

Note that in the proposed model, the velocity pulse is deterministic while the high frequency content is treated as a realization of a stochastic process defined by the deterministic modulating function $A_n(t)$, randomly generated phase angles ϑ_k and frequency coefficients B_k . An iterative procedure that is based on the SIMQKE algorithm described by Gasparini [5] is used to find the coefficients B_k . In particular, these coefficients are determined such that the mean displacement response spectrum of the ensemble of ground motions generated by (9) approximately matches a target displacement response spectrum. A detailed description of the procedure used to find B_k can be found in Menuin [6].

Verification

For each near-fault ground motion listed in Tables 1a and 1b ($i = 1, 2, \dots, 52$), 20 simulated ground motions, $a_{sij}(t) = a_{pi}(t) + a_{nij}(t)$, $j = 1, 2, \dots, 20$, were generated using (9), where $a_{pi}(t)$ is the acceleration time history associated with the velocity pulse fitted to the i th recorded ground motion and $a_{nij}(t)$ is the j th realization of the high frequency accelerations obtained for a random realization of the phase angles ϑ_k in (9). To generate the simulations for the i th ground motion, the shape parameter β used in the definition of $A_n(t)$ was computed using (8) with the Arias duration of the recorded ground motion and the frequency coefficients B_k in (9) were calibrated to match the response spectrum of the record.

To assess the suitability of the proposed simulation procedure for structural analyses, we consider the response of an SDOF system to the recorded ground motions and their simulations described above. The oscillator has initial stiffness k_0 , yield strength f_y , post-yield stiffness $k_0/10$ and damping ratio $\zeta=0.03$. The

ductility ratio of the system is defined as $\mu = \delta_{\max}/\delta_y$, where δ_{\max} is the maximum absolute displacement of the oscillator when it is excited by a ground motion and $\delta_y = f_y/k_0$ is the displacement at which the oscillator first yields. For an oscillator that has initial natural period T , let $\delta_{y,gi}(T,\mu)$ denote the required yield displacement of the system such that the ductility ratio is μ when the oscillator is subjected to i th recorded ground motion listed in Tables 1a and 1b. Similarly, let $\delta_{y,sij}(T,\mu)$, $\delta_{y,pi}(T,\mu)$ and $\delta_{y,nij}(T,\mu)$ denote the required yield displacements when the oscillator is subjected to $a_{sij}(t)$, $a_{pi}(t)$ and $a_{nij}(t)$, respectively. A plot of $\delta_{y,gi}(T,\mu)$, $\delta_{y,pi}(T,\mu)$, $\delta_{y,nij}(T,\mu)$ or $\delta_{y,sij}(T,\mu)$ as a function of T for a prescribed value of μ is known as a constant ductility response spectrum.

We assess the ability of the proposed simulation procedure to reproduce the important characteristics of a fault-normal near-fault ground motion by computing the response ratio

$$\psi_{sij}(T,\mu) = \delta_{y,sij}(T,\mu) / \delta_{gi}(T,\mu) \quad (10)$$

for each simulated ground motion. It should be apparent that when $\psi_{sij}(T,\mu) = 1$ the simulated ground motion predicts displacement demands that are equal to those caused by the recorded ground motion that the simulation is based upon. Previous studies (Menun [1] and Alavi [7]) suggest that the response of nonlinear SDOF and MDOF systems to fault-normal near-fault ground motions is sensitive to the ratio $\gamma = T/T_p$. Consequently, it is useful to rewrite (10) as

$$\psi_{sij}(\gamma T_{pi}, \mu) = \delta_{y,sij}(\gamma T_{pi}, \mu) / \delta_{gi}(\gamma T_{pi}, \mu) \quad (11)$$

where T_{pi} is the velocity pulse period found for the i th ground motion. The sample mean for the response ratio defined by (11),

$$\bar{\psi}_s(\gamma, \mu) = \frac{1}{52} \sum_{i=1}^{52} \left[\frac{1}{20} \sum_{j=1}^{20} \psi_{sij}(\gamma T_{pi}, \mu) \right], \quad (12)$$

which includes all ground motions ($i = 1, 2, \dots, 52$) and all simulations ($j = 1, 2, \dots, 20$) for each ground motion, is plotted in Figure 5 as a function of γ . To better understand the accuracy and limitations of the proposed model, it is also useful to consider the response ratios associated with the fitted velocity pulses,

$$\psi_{pi}(\gamma T_{pi}, \mu) = \delta_{y,pi}(\gamma T_{pi}, \mu) / \delta_{gi}(\gamma T_{pi}, \mu), \quad (13)$$

and the high frequency accelerations,

$$\psi_{nij}(\gamma T_{pi}, \mu) = \delta_{y,nij}(\gamma T_{pi}, \mu) / \delta_{gi}(\gamma T_{pi}, \mu). \quad (14)$$

The sample mean curves for these response ratios are also plotted in Figure 5 as a function of γ . As indicated in Figure 5, the velocity pulse model (without the high frequency accelerations superimposed upon it) causes displacement demands that are comparable to the recorded near-fault ground motions when $\gamma > 0.65$; however, it underestimates displacement demands when $\gamma < 0.65$ (short periods). In contrast, the displacement demands caused by the high frequency accelerations (without the accelerations associated with the velocity pulse) are comparable to those caused by the recorded ground motions when $\gamma < 0.65$, but underestimate the displacement demands when $\gamma > 0.65$. However, when the simulated high frequency accelerations are superimposed on the velocity pulse model, the sample mean is close to unity for all values of γ ; i.e., the proposed simulation procedure generates acceleration time histories that, on average, cause displacement demands in the nonlinear SDOF system that are comparable to that caused by the recorded near-fault ground motions at all periods and ductility demand levels.

Estimating the target response spectrum

The simulations used to generate the results plotted in Figure 5 utilized the response spectra of the original records to calibrate the frequency coefficients in (9). In reality however, a target response spectrum for a given seismic environment is required to implement the above simulation procedure. The proposed model assumes that a fault-normal near-fault ground motion consists of a velocity pulse, $a_p(t)$, and high frequency content, $a_n(t)$, that, based on the results presented in Figure 5, are well separated in the frequency domain; i.e., $a_p(t)$ dominates at long periods and $a_n(t)$ dominates at short periods. Consequently,

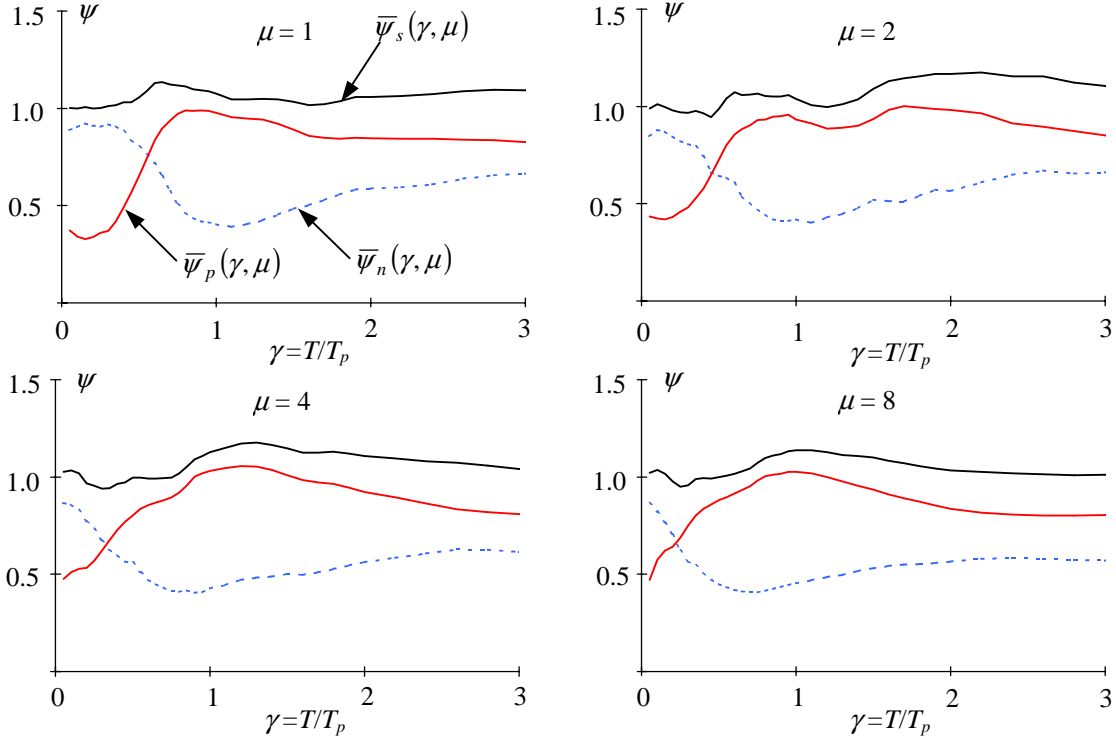


Figure 5. Response ratio curves for $1 \leq \mu \leq 8$.

if we can obtain estimates for the response spectra $Sa_p(T, \zeta)$ and $Sa_n(T, \zeta)$ associated with $a_p(t)$ and $a_n(t)$, respectively, then it is reasonable to construct the target response spectrum, $Sa_s(T, \zeta)$, needed to estimate the frequency coefficients in (9) by an square-root-sum-of-squares (SRSS) rule; i.e.,

$$Sa_s(T, \zeta) = \sqrt{[Sa_p(T, \zeta)]^2 + [Sa_n(T, \zeta)]^2}. \quad (15)$$

This rule assumes that the peak displacement caused by $a_p(t)$ is uncorrelated in time with the peak displacement caused by $a_n(t)$. Figure 6 presents comparisons of $Sa_s(T, \zeta)$ computed using (15) to the recorded response spectrum, $Sa_g(T, \zeta)$, for four representative ground motions. It is apparent from this figure that $Sa_s(T, \zeta)$ is in good agreement with $Sa_g(T, \zeta)$. As expected, the largest differences between $Sa_s(T, \zeta)$ and $Sa_g(T, \zeta)$ occur at those periods at which $a_p(t)$ and $a_n(t)$ make comparable contributions to the response. However, the procedure does not appear to be biased since $Sa_s(T, \zeta)$ over-predicts $Sa_g(T, \zeta)$ for some records and under-predicts $Sa_g(T, \zeta)$ for others. Procedures for estimating $Sa_p(T, \zeta)$ and $Sa_n(T, \zeta)$ needed to compute $Sa_s(T, \zeta)$ for a given seismic environment are described below.

PREDICTIVE RELATIONSHIPS FOR GROUND MOTION MODEL PARAMETERS

Predictive relationships for velocity pulse model

In this section, we develop relationships that can be used to predict the model parameters T_p , V_p and α that define $a_p(t)$ for a given seismic environment. We remark that the parameter t_0 only serves to locate the start of the pulse along the time axis; consequently, the only criteria an analyst need consider when specifying t_0 is that $t_0 = 0$ and large enough that the high frequency modulating function $A_n(t)$ defined by (7) is close to zero at $t = 0$.

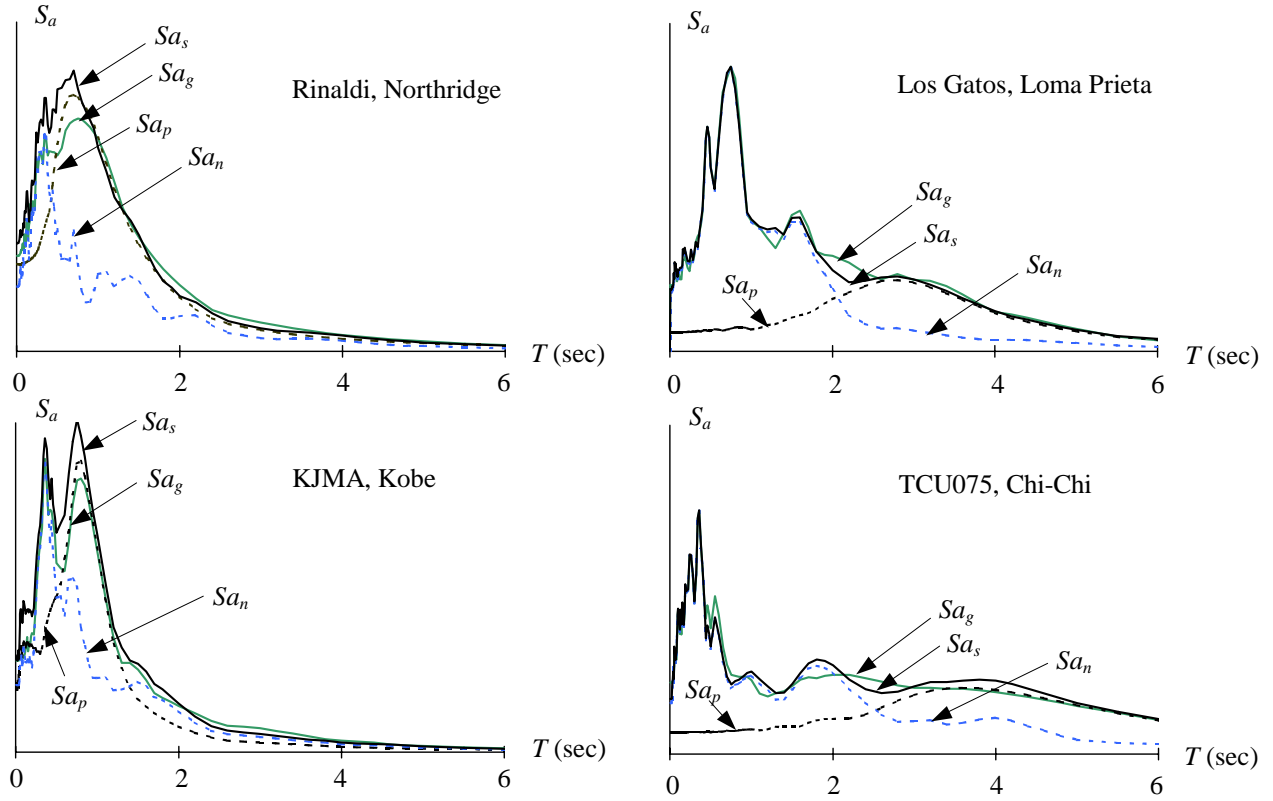


Figure 6. Examples of the SRSS rule.

Velocity Pulse Amplitude, V_p

Several studies have noted that the peak ground velocity (PGV) observed at a site during an earthquake is dependent upon the magnitude (M_w), distance (R), and site conditions. In particular, Alavi [7], Rodriguez-Marek [8] and Somerville [9] have performed regression analyses to relate PGV to M_w and R in the near-fault zone using different sets of recorded ground motions. Based on the 52 near-fault ground motions we have included in this study, we propose

$$\log_{10} \text{PGV} = 0.49 + 0.21M_w - 0.16\log_{10} R. \quad (16)$$

The data summarized in Tables 1a and 1b suggests that a strong correlation exists between V_p and PGV, which is a reasonable observation when one considers the role that V_p plays in (1). A regression analysis of the data listed in Tables 1a and 1b yields $V_p = 0.80\text{PGV}$, which when combined with (16) allows us to express V_p in terms of M_w and R as

$$\log_{10} V_p = 0.39 + 0.21M_w - 0.16\log_{10} R. \quad (17)$$

Velocity Pulse Period, T_p

Figure 5 indicates that T_p has a significant effect on the structural response, particularly when $T/T_p \approx 1$. Consequently, a realistic pulse period is critical if the proposed ground motion model is to be used in dynamic analyses. When fitting the proposed velocity model to the ground velocity generated by the Haskell source model (Figure 1), we found that T_p is related to the rise time, t_r , assumed in the Haskell model. Based on this observation and those made by Somerville [10], who noted a relationship between the rise time and magnitude of an earthquake, it is reasonable to assume that T_p is related to M_w . Using the 52 near-fault ground motions included in this study, the following empirical relationship was derived

$$\log_{10} T_p = -3.38 + 0.54M_w. \quad (18)$$

This regression, which is shown in the Figure 7a, indicates that there is a strong dependence between T_p and M_w . Also plotted in this figure are the regressions for rock and soil conditions, which indicate that the relationship between T_p and M_w is different for these site conditions at small magnitudes but the difference disappears as M_w increases. We remark that similar empirical relationships between pulse period and magnitude have also been proposed by Alavi [7], Rodriguez-Marek [8] and Somerville [11], but with different definitions for the period of the pulse and different data sets.

Velocity Pulse Shape Parameter, α

The shape parameter α influences both the waveform of the velocity pulse (a time domain characteristic) and the width and location of the spectral content (frequency domain characteristics). When α is assigned a large absolute value, the length of the signal in the time domain increases but the bandwidth of the frequency content decreases. Plotting the absolute values of α against the values of T_p obtained for the ground motions listed in Table 1a and 1b reveals the empirical relationship

$$|\alpha| = \frac{2.5}{T_p}, \quad (19)$$

which is shown in Figure 7b. This observation suggests that once T_p is estimated using (18), a realistic value of α can be obtained from (19).

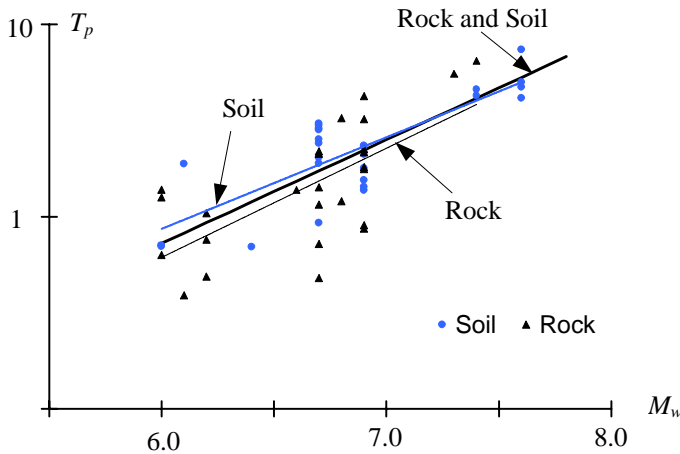


Figure 7a. Relationship between M_w and T_p .

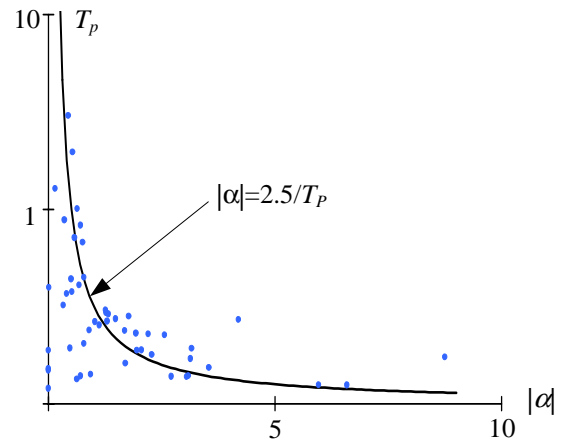


Figure 7b. Relationship between α and T_p .

Predictive relationships for high frequency content

Recall that the high frequency content introduced into a simulated record is a realization of a stochastic process (6). In addition to the randomly generated phase angles, ϑ_k , the model requires as input a shape parameter β and frequency coefficients B_k .

High frequency shape parameter, β

The shape parameter β , which controls the rate at which the intensity of the high frequency accelerations grow and decay over time is related to the Arias duration of the ground motion as indicated by (8). Consequently, for a given seismic environment, an appropriate value for β may be estimated using available attenuation relationships for Arias duration, such as that proposed by Abrahamson [12], and substituting the predicted Arias duration into (8). We remark that, based on the analyses that we have performed thus far with the proposed procedure, the quality of the simulated ground motions appears to be insensitive to small perturbations in β .

Frequency coefficients, B_k

Recall that the frequency coefficients assumed in (6) and (9) are calibrated to match a target response spectrum, which is generated by combining the response spectrum associated with the velocity pulse, $Sa_p(T, \zeta)$, with the assumed response spectrum associated with the high frequency content, $Sa_n(T, \zeta)$, by means of the SRSS rule (15). We remark that once the parameters of the velocity pulse model have been assigned, $Sa_p(T, \zeta)$ is readily available. To specify $Sa_n(T, \zeta)$, we utilize the empirical response spectral attenuation relations without the directivity modification developed by Abrahamson [13].

To investigate the suitability of this approach for specifying $Sa_n(T, \zeta)$, the Abrahamson and Silva attenuation relationship was used to predict the mean response spectrum associated with the magnitude, distance, faulting mechanism, and site condition of each ground motion listed in Tables 1a and 1b; i.e., 52 response spectra, corresponding to the 52 ground motions listed in Tables 1a and 1b were predicted. In Figure 8, the ensemble statistics of these predicted response spectra are plotted against the ensemble statistics of the response spectra computed for the recorded high frequency content of the ground motions. It is clear from this figure that a bias is present in the predicted spectra. To understand the source of this bias, it is instructive to compute the response spectrum ratio

$$\psi_{Sa,i}(T, \zeta) = \frac{Sa_{n,i}(T, \zeta)}{Sa_{A\&S,i}(T, \zeta)} \quad (20)$$

for each ground motion ($i = 1, 2, \dots, 52$), where $Sa_{n,i}(T, \zeta)$ and $Sa_{A\&S,i}(T, \zeta)$ are the recorded and predicted response spectra, respectively.

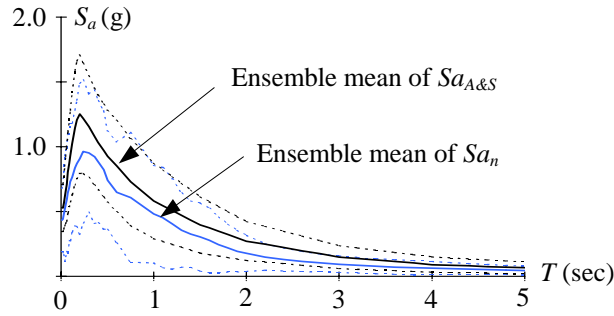


Figure 8. Ensemble statistics of Sa_n and $Sa_{A\&S}$.

The average response spectrum ratio

$$\bar{\psi}_{Sa}(T, \zeta) = \frac{1}{N} \sum_{i=1}^N \psi_{Sa,i}(T, \zeta) \quad (21)$$

for rock ($N = 26$) and soil ($N = 26$) site conditions are shown in Figure 9, in which it is apparent that the bias varies with spectral period. For the soil site condition, the bias is small at short periods but becomes significant for intermediate and long periods. For the rock site condition, the bias fluctuates slightly with the period; however, an obvious trend like that observed for the soil sites is not apparent. To correct the bias noted in the predicted response spectra in Figure 8, we propose the piecewise-linear correction functions plotted in Figure 9 for rock and soil site conditions.

SIMULATIONS BASED ON THE PREDICTIVE RELATIONSHIPS

The objective of the proposed simulation procedure is to generate near-fault ground motions for a given seismic environment. With the predictive relationships for the ground motion model parameters established in the previous section, we are now able to simulate the fault-normal near-fault ground motion for an arbitrary site.

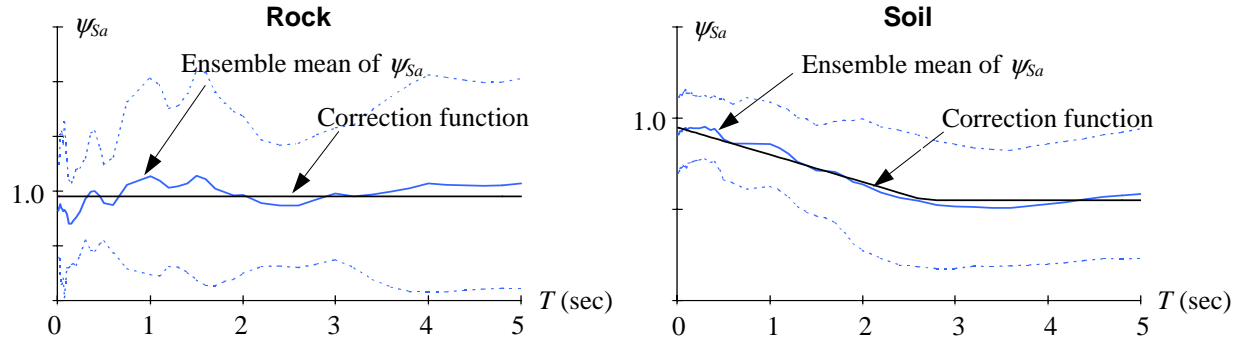


Figure 9. Ensemble mean of response spectrum ratio's ψ_{Sa} and correction functions.

For each ground motion listed in Tables 1a and 1b, the magnitude, distance, faulting mechanism and site conditions were used to predict the model parameters of the velocity pulse and the high frequency accelerations using the empirical relationships presented in the previous section. The predicted response spectrum for each record was then generated using the SRSS rule (15). Figure 10 compares the ensemble statistics of these predicted response spectra with those of the recorded response spectra. Studying this figure, we see that for periods $T > 1.5$ s the ensemble mean of the predicted response spectra matches that of the recorded response spectra. However, for periods $T < 1.5$ s, discrepancies as large as 20% between the ensemble means can be seen. Figure 10 also indicates that the variation of the predicted response spectra is less than that of the recorded response spectra at all periods. This reduced variability is due to the fact that when we estimated the model parameters using (17), (18) and (19), we ignored the aleatory variability present in the regression analyses used to derive these empirical relationships; e.g., for a given magnitude event, all simulations have the same pulse period T_p and shape parameter α , since T_p (and hence α) is only a function of M_w in (18). We remark that ignoring the aleatory variability when predicting the model parameters may also be partially responsible for the observed discrepancies between the ensemble means. Probabilistic models for the model parameters that account for the scatter of the data present in Figures 7a and 7b may be more appropriate than the deterministic relationships used to generate the response spectra plotted in Figure 10.

Using the predicted response spectra computed above as targets, ground motion time histories for earthquakes of different magnitudes were simulated using (9). Figure 11 presents the simulated ground velocities on rock condition for three events of different magnitudes and their corresponding response spectra. Note that, in contrast to the current provisions of the Uniform Building Code [14] that stipulate a monotonically increasing spectral amplitude with increasing magnitude for all periods, the amplitudes of the simulated response spectra do not increase monotonically with magnitude; the spectral shape of the simulated near-fault ground motions is magnitude dependent at intermediate and long periods.

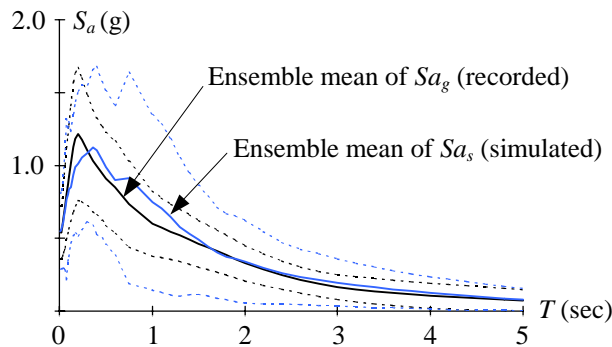


Figure 10. Ensemble statistics of Sa_g and Sa_s .

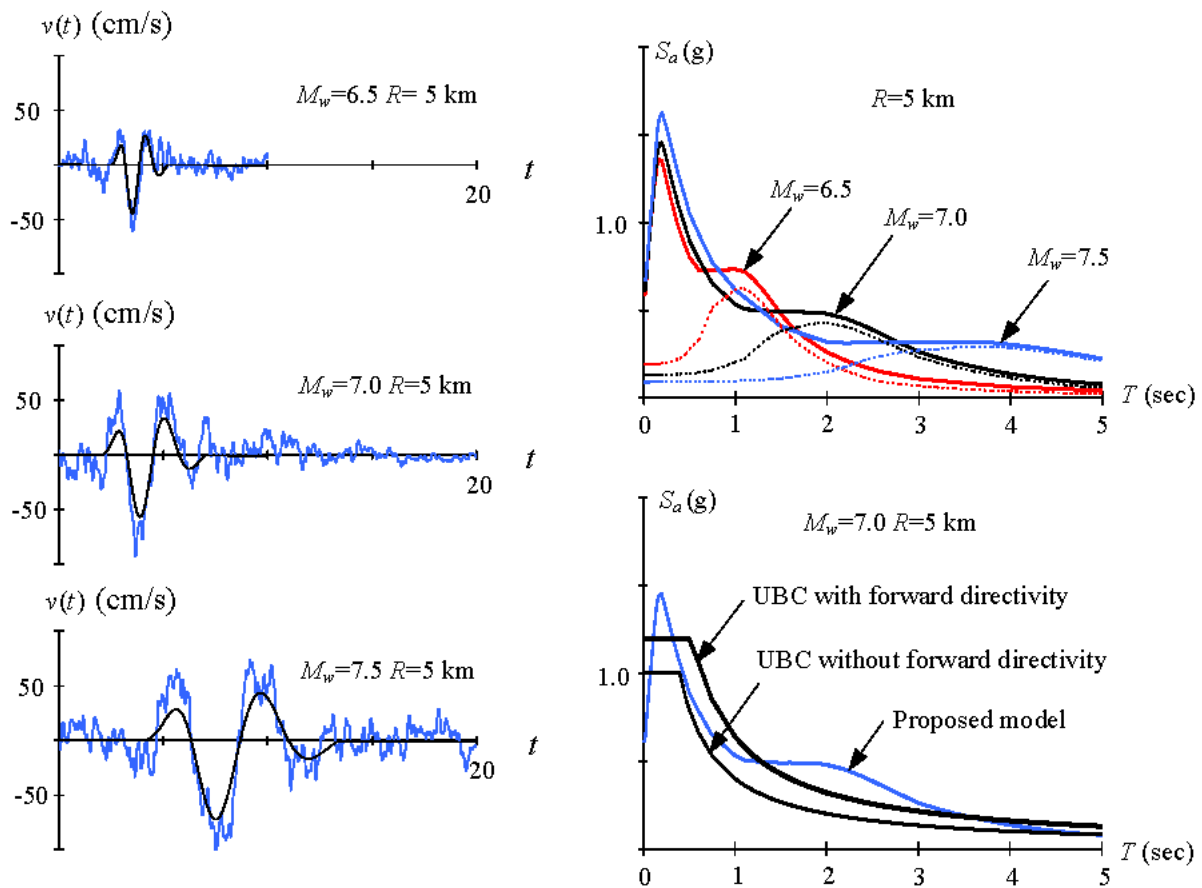


Figure 11. Simulated fault-normal near-fault ground velocities, their response spectra and UBC-97 code provisions for near fault S_a with soil type S_B .

CONCLUSIONS

In this paper, a fault-normal near-fault ground motion simulation procedure, which complements the current state of practice by providing engineers with ground motions that are representative of the near-fault environments when recorded ground motions are not available, is described. The proposed procedure constructs a simulated fault-normal near-fault accelerogram by superimposing a realization of nonstationary high frequency accelerations obtained from a stochastic model on to the acceleration time-history associated with a deterministic model of the velocity pulse commonly observed in such ground motions.

To generate a simulated ground motion with the proposed procedure, the analyst must specify the values of several model parameters that control the temporal and frequency domain characteristics of the ground motion. Empirical relationships that can be used to predict appropriate values for the model parameters for a given seismic environment (magnitude and distance of the earthquake and the site soil conditions) are derived from regression analyses performed on an ensemble of 52 recorded fault-normal near-fault ground motions. Available attenuation relationships for response spectrum ordinates and Arias duration are also used to specify the high frequency content of the simulated records.

The ability and limitations of the proposed simulation procedure are examined by comparing the displacement demands in linear and nonlinear single-degree-of-freedom systems caused by the ensemble of recorded ground motions and their simulations. In general, it was found that the ensemble means of the simulated and recorded response spectra agree at periods $T > 1.5$ s. However, discrepancies as large as 20% were observed for $T < 1.5$ s. It was also noted that the variability in the predicted spectral ordinates about the ensemble mean was less than that seen in the recorded ground motions. This reduction in the variability is attributed to the fact that the scatter of the data present in the regression analyses used to derive the empirical predictive relationships for the model parameters was ignored. This observation suggests that probabilistic models that can properly account for inherent variability present in the model parameters may be more appropriate than the deterministic equations used to predict the model parameters in this paper.

REFERENCES

1. Menun, C. and Fu, Q (2002). "An analytical model for near-fault ground motions and the response of SDOF systems." Proc. of the 7th U.S. National Conf. on Earthquake Engineering, Boston, MA.
2. Mavroeidis, G.P. and Papageorgiou, A.S. (2002). "Near-source strong motion: characteristics and design issues." Proc. of the 7th U.S. National Conf. on Earthquake Engineering, Boston, MA.
3. Somerville, P.G., Smith, N.F., Graves, R.W., and Abrahamson, N.A. (1997). "Modification of empirical strong ground motion attenuation relations to include the amplitude and duration effects of rupture directivity." *Seismological Research Letters*, 68, p199-222.
4. Aki, K. and Richards, P.G. (1980). "Quantitative Seismology: Theory and Methods." W.H. Freeman and Company, New York.
5. Gasparini, D., and Vanmarcke, E.H. (1976). "Simulated earthquake motions compatible with prescribed response spectra." Evaluation Seismic Safety of Buildings Report No.2, Dept. of Civil Engineering, M.I.T., Cambridge, MA.
6. Menun, C. and Kiureghian, A.D. (1999). "Envelopes for seismic response vectors." Report No. UCB/PEER 1999/08, Earthquake Eng. Research Center, University of California, Berkeley, CA.
7. Alavi, B. and Krawinkler, H. (2000). "Consideration of near-fault ground motion effects in seismic design." Proc. of the 12th World Conf. on Earthquake Engineering, Auckland, New Zealand.
8. Rodriguez-Marek, A. (2000). "Near-fault seismic site response." Ph.D. Dissertation, Dept. of Civil Engineering, University of California, Berkeley.
9. Somerville, P.G. (1998). "Development of an improved representation of near-fault ground motions." Proc. of SMIP98 Seminar on Utilization of Strong Motion Data, California Strong Motion Instrumentation Program, Sacramento, CA.
10. Somerville, P.G., Irikura, K., Graves, R.W., Sawada, S., Wald, D., Abrahamson, N.A., Iwasaki, Y., Kagawa, T., Smith, N., and Kowada, A. (1999). "Charactering crustal earthquake slip models for prediction of strong ground motion." *Seismological Research Letters*, 68, p199-222.
11. Somerville, P.G. (2003). "Magnitude scaling of near fault rupture directivity pulse." *Physics of the Earth and Planetary Interiors*, 137, p201-212.
12. Abrahamson, N.A. and Silva, W.J. (1996). "Arias duration of horizontal shaking attenuation relationships." Written Communication.
13. Abrahamson, N.A. and Silva, W.J. (1997). "Empirical response spectral attenuation relations for shallow crustal earthquakes." *Seismological Research Letters*, 68, p94-127.
14. International Conference of Building Officials (1997) Uniform Building Code. Whittier, CA.